Petroleum Science 23 (2026) 4364–4379

Contents lists available at ScienceDirect

Petroleum Science

journal homepage: www.keaipublishing.com/en/journals/petroleum-science

Original Paper

Planning and operation optimization for oilfield negative carbon integrated energy system considering source-load interaction

Zhi-Hui Gao [a,b], Ding-Ding Wang [a,b], Jiang-Feng Liu [c,d], Shao-Jie Hao [a,b], Qi Zhang [a,b,*]

[a] School of Economics and Management, China University of Petroleum (Beijing), Beijing, 102249, China
[b] School of Business Administration, China University of Petroleum-Beijing at Karamay, Karamay, 834000, Xinjiang, China
[c] School of Management, Beijing Institute of Technology, Beijing, 100081, China
[d] Center for Energy and Environmental Policy Research, Beijing Institute of Technology, Beijing, 100081, China

ARTICLE INFO

Article history:
Received 1 May 2025
Received in revised form
10 November 2025
Accepted 14 January 2026
Available online 21 January 2026

Edited by Min Li

Keywords:
Oilfield integrated energy systems
Negative carbon
Energy transition
Source-load interaction
Planning and operational optimization

ABSTRACT

Towards the carbon neutrality, the traditional fossil fuel-based energy supply in oilfield urgently needs to be replaced by the integrated energy systems (IES) based on zero carbon and negative carbon technologies. However, existing studies have not yet to address the challenge of optimization design for negative carbon IES under flexible load conditions in oilfield. Therefore, three scenarios are proposed in the present study, an IES integrating renewable energy and negative carbon technology (Case 2), further incorporating source-load interaction (Case 1) and the conventional energy system (Case 3). A planning and operational optimization model are developed to validate the advancement of the system and the effectiveness of the source-load interaction mechanism. The obtained results show that: i) The oilfield IES increases net present value (NPV) by 10.26% and 1.35% in Case 1 and Case 2 comparing with Case 3 respectively, supporting a cost-effective transition. ii) All three scenarios realize negative-carbon operation, and the net emission reductions of Case 1 and Case 2 are 9.20% and 8.20% higher respectively comparing with Case 3. iii) The Case 1 with source-load interaction improves the performance in economic, decarbonization and reliability by 9.04%, 1.00% and 6.67% respectively compared to the Case 2. Therefore, the present study offers a more efficient solution to the trilemma in the low-carbon transition in oilfield energy system.

1. Introduction

In response to the escalating global climate crisis, carbon reduction efforts have entered a critical phase of acceleration. The Sixth Assessment Report of the Intergovernmental Panel on Climate Change (IPCC) asserts that “rapid and deep reductions in greenhouse gas emissions require major energy system transitions” (IPCC, 2023). Oil production, a significant energy provider and major energy consumer, plays a crucial role in this transition. In 2022, the production, transportation, and processing of oil and gas generated 5.1 billion tons of carbon dioxide (CO_2)-equivalent emissions, accounting for nearly 15% of global energy-related greenhouse gas emissions (IEA, 2023). Amid increasing decarbonization pressures, the oil and gas industry is undergoing a technology-driven energy transition centered on “clean energy substitution”. Leading energy companies, including China National Petroleum Corporation (CNPC, 2022), Total Energy (Total Energy, 2022), Shell Petroleum (Shell Petroleum, 2023), have initiated new energy-powered oilfield projects integrating wind and solar energy. The use of renewable energy resources will save significant amounts of resources such as gas, freeing them to meet the energy demand for other applications, as well as reducing the environmental impact of the industry (Absi Halabi et al., 2015).

Unlike conventional industrial sectors, oilfield production features a unique combination of rigid thermal loads, flexible electrical loads, and multi-energy coupling. Continuous high-temperature heating is indispensable for maintaining crude fluidity and pipeline safety, while pumping and auxiliary electromechanical equipment can be modulated or shifted to follow renewable output. Moreover, the delayed dissolution and migration of injected CO_2 create a schedulable demand component on daily to weekly scales (Ma et al., 2022). System configuration plays

* Corresponding author.
E-mail address: ZhangQi56@tsinghua.org.cn (Q. Zhang).

Peer review under the responsibility of China University of Petroleum (Beijing).

https://doi.org/10.1016/j.petsci.2026.01.019
1995-8226/

a decisive role in the performance of energy systems, and the integrated devices are strongly correlated with the specific energy utilization scenario of the oilfield integrated energy systems (IES) itself (Ao et al., 2025). Consequently, oilfield IES must simultaneously meet electricity, heat, and CO_2 supply requirements, with energy demands across different production stages, resulting in highly complex load dynamics. Although multi-energy systems are increasingly recognized as effective for industrial decarbonization (Wang et al., 2024a), the intermittency and variability of wind and solar generation lead to it alone cannot meet the oilfield multi-dimensional load. The coal-fired combined heat and power (CHP) units equipped with CCS provide a transitional pathway (An et al., 2025; Fan et al., 2023; Wang et al., 2025), which can deliver both baseload and peak-shaving power (Lu et al., 2021) while simultaneously supplying stable thermal energy and CO_2 stream (Wang et al., 2024b).

The deployment of renewable energy, CHP, and CCS technologies in oilfields still faces persistent challenges (Zhang et al., 2023a). These include the complexities of multi-source integration, lack of source-load interaction, and market price fluctuations (Zhao et al., 2025; Zhang et al., 2022; Gu et al., 2020). These shortcomings highlight the limitations of merely stacking low-carbon technologies without optimizing synergies across energy sources. Moreover, fluctuating electricity prices, seasonal industrial CO_2 pricing, and evolving carbon trading frameworks further influence oilfield energy strategies (Zhang et al., 2023c). Addressing these challenges necessitates a shift toward IES that harmonize energy supply, transmission, and consumption. Meanwhile, oilfields urgently need to upgrade the high carbon supply model by embracing renewable and flexible energy solutions.

Currently, the IES has increasingly become a research focus in the energy sector. They improve energy efficiency, foster energy savings, and reduce emissions by optimizing the use of multiple energy sources (Mancarella, 2014). Numerous studies have been conducted in industries with diverse and high energy consumption, such as coal mining, steel manufacturing, and chemical industries. For instance, Hu et al. (2022) proposes a coal mine energy system integrating byproduct energy and flexible load dispatch, using multi-objective optimization to balance economy, environment and demand, enabling sustainable mining. Lin et al. (2023) develops a park-level energy system with hydrogen chain, optimizing multi-timescale storage and multi-pressure-ratio compressors, achieving carbon reduction, cost savings and operational flexibility for hydrogen integration. Gan et al. (2023) develops a park-level IES integrating hydrogen-based blast furnace and electric arc furnaces technologies. With dynamic carbon pricing, the model demonstrates strong decarbonization potential, offering forward-looking solutions for steel industry transition. In recent years, source-load interaction mechanisms have been widely considered in scheduling due to their high flexibility, fast response time, and environmental benefits. Core techniques include demand-side management (Sarker et al., 2020), distributed energy (Qin et al., 2019), virtual power plants (Li et al., 2024; Machado et al., 2024), flexible load (Liu et al., 2025), and cross-regional coordinated dispatch (Zhang et al., 2024). By optimizing source-load interaction, energy wastage can be minimized while ensuring system stability, ultimately improving energy utilization efficiency.

The modeling and scheduling of IES for various application scenarios have been well explored. However, the oilfield IES, a typical energy producer and high-consumption industry, remains under-researched. Oilfield production processes involve multiple energy-intensive stages, such as steam injection, well heating, and pumping (Cao et al., 2020). Flexible production systems that enable load shifting and scheduling within defined limits are emerging as key strategies for achieving low-carbon transformations in oilfields. By integrating renewable energy sources like wind, solar, and geothermal energy into the oilfield energy supply system, the reliance on fossil energy can be reduced, lowering carbon emissions. For example, Li et al. (2024a) proposes a polycyclic conjugated hydrocarbons (PCHs)-based solar-gas heating system, reducing gas use by 7.02% versus water storage, with optimal efficiency when phase-change temperature is slightly below demand (80 °C→62 °C cuts boiler demand by 75.60 GJ). Zhang et al. (2021) develops an offshore energy system model, proving wind power integration reduces emissions by 39.91% and costs by 2.57%, identifying 57.04% as optimal wind penetration, supporting offshore oilfield decarbonization decisions. Xu et al. (2023) develops an oil-water thermal-flow model and optimizes geothermal-oil cogeneration in abandoned wells using NSGA-II (Non-dominated Sorting Genetic Algorithm II). The optimized scheme boosts economic benefits by \$6.75M and outlet temperature by 7.10 K over 15 years. Nevertheless, reliance on a single renewable energy source is insufficient to meet the continuous and stable energy demands of oilfields. Consequently, many oilfields are combining multiple carbon-neutral technologies to achieve both stable energy supply and low-carbon emission reduction goals. For instance, Peng et al. (2025) pioneers an Oilfield IES optimization model integrating CHP-CCS-PTSF (Photovoltaic-Thermal Storage Furnace) units, which employs IGDT (Information gap decision theory) to address source-load uncertainties. Achieving 75.11% emission reduction and over 95% renewable utilization rates. Li et al. (2025) proposed an integrated framework for oilfield energy transition that incorporates a multi-energy integration model with microgrids and heating pipelines, demonstrating in a case study a 30.41% reduction in total costs and a 24.23% decrease in carbon emissions compared with conventional systems.

As multi-energy coupling technologies are progressively applied, achieving IES planning while maintaining energy balance has become another important research direction. Current research has been widely applied to multi-energy systems configuration optimization (Ma et al., 2024; Yang et al., 2022; Zhang et al., 2023b), operational optimization (Chai et al., 2023; James et al., 2016), and dispatch optimization (Li et al., 2015; Sima et al., 2024). However, research on integrated energy systems for oilfields remains limited. As shown in Table 1, existing works either focus on park-level IES, or, when involving oilfields, simplify production loads and overlook the dynamic coupling among steam injection, oil extraction, and gathering-transport processes. In addition, most studies treat capacity planning and operational scheduling separately, lacking a framework that coordinates long-term investment with short-term operational flexibility. Therefore, under carbon-neutrality targets and fluctuating renewable conditions, there is a clear need for an oilfield-oriented model that captures source-load interaction and supports integrated planning-operation optimization.

To address persistent research gaps and the urgent low-carbon transition needs in oilfield production, we propose a negative-carbon integrated energy system (NC-IES). The system is grounded in an electricity-heat-carbon load model that distinguishes rigid thermal demand from flexible electrical demand, avoiding the conventional constant-load assumption. On this basis, we develop a multi-objective, cross-scale optimization framework that couples capacity planning with hourly operational dispatch, ensuring consistent decisions across the planning-operation lifecycle. This framework jointly enhances cost performance, carbon reduction, and operational reliability, providing a practical pathway to resolve the oilfield energy trilemma and align investment strategy with real time field operations.

Table 1
Review of integrated energy system studies.

Author	Application scenario	System boundary	Objective	Source-load interaction considered
Peng et al. (2025)	Oilfield IES	CHP, CCS, PV-thermal-storage-electric boiler system	Dispatch optimization	✓
Wang et al. (2022)	Oilfield IES	PV, CHP	Dispatch optimization	✓
Li et al. (2024b)	Oilfield heating system	Solar energy, geothermal energy, thermal Storage	Simulation analysis	×
Lin et al. (2025)	Coal mine IES	PV, wind power, gas combustion engine, heat pump, energy storage	Capacity planning	×
Qian et al. (2025)	IES	PV, electrolyze, methanation reactor, hydrogen fuel cell, energy storage	Capacity planning	×
Li et al. (2023)	IES	PV, wind power, shared hydrogen storage	Capacity + operational optimization	×
Zhang et al. (2021)	Offshore oilfield IES	Wind power, district heating network	Capacity + operational optimization	×
Ma et al. (2024)	IES	PV, coal-fired power generation	Capacity planning	×
Zhang et al. (2023a, b, c)	IES	Wind power, PV, coal power, CCS	Capacity planning	×

2. Methodology

The model framework is illustrated in Fig. 1. In step 1, a collaborative renewable energy-CHP-CCUS (RC-CCUS) is proposed through refined equipment modeling. Specifically, the CHP unit feeds pulverized coal into a boiler to generate high-pressure steam, part of which drives turbines for power generation while the remainder is extracted for district heating, enabling thermoelectric decoupling. Flue gas undergoes desulfurization and denitrification before CO_2 is captured using a lean/rich amine absorption–desorption process. Photovoltaic arrays and wind turbines are integrated via inverters and transformers, with their intermittency dynamically balanced by the CHP's peak-shaving flexibility to form a stable hybrid energy supply system. The captured CO_2 is transported for EOR in nearby fields, while the system collectively satisfies both baseload and peak demand. In Step 2, cost and revenue parameters are identified across the RC-CCUS workflow. In Step 3, a nonlinear optimization model is formulated to co-optimize annual installed capacities of PV, wind, CHP, and CCUS alongside real time electricity, heat, and carbon flows. The model integrates coordinated annual and hourly operation strategies, incorporating granular variables such as PV, wind, and CHP generation, CO_2 injection and oil production, and external CO_2 procurement. Finally, the framework is applied to derive optimal planning and operation schemes under alternative scenarios, thereby evaluating system performance in terms of economic viability, decarbonization, and reliability.

2.1. Assumptions

The following are the assumptions of the integrated planning-operation optimization model:

I. The model spans a twenty-year planning horizon, including a one-year construction phase. Equipment expansion costs are depreciated over the 20th year for cost recovery (Lin et al., 2025).
II. The system prioritizes internal electricity consumption for production, excluding surplus electricity from grid feed-in. Seasonal industrial heat demand is considered, and the CHP system supplies high-pressure steam for external heating.
III. All CO_2 emissions from the CHP system are used for EOR processes. Any CO_2 deficit is supplemented through market procurement, assuming sufficient supply capacity in the industrial CO_2 market.
IV. The model is applied to a new CO_2-EOR project in an oilfield in Xinjiang, China, using an ultra-supercritical indirect air-cooled coal-fired CHP unit. A 20-year oil production and CO_2 injection plan is considered, assuming homogeneous oil wells with identical production and injection characteristics.

2.2. Oilfield IES planning and operational optimization model

2.2.1. Photovoltaic model

The maximum output power of the PV system at time t, denoted as $p_{pv,t}$, is calculated as expressed in Eq. (1):

$$p_{pv,t} = I_{tilted,t} \times A_{module} \times \eta_{module} \times f_{pv,system} \tag{1}$$

where $I_{tilted,t}$ is the solar irradiance on the tilted surface at time t, A_{module} is the total area of the PV modules, η_{module} is the module conversion efficiency, and $f_{pv,system}$ is the overall loss factor.

$$A_{module} = \frac{c_{pv}}{p_{module}} \times A_{panel} \tag{2}$$

where c_{pv} is the total installed capacity of the PV system, p_{module} is the power generation capacity of a single module, and A_{panel} corresponds to the surface area of a single module. The solar irradiance on the tilted surface is determined by the direct normal irradiance (DNI), diffuse horizontal irradiance (DHI), and global horizontal irradiance (GHI).

$$I_{tilted,t} = \mathrm{DNI}_t \times \cos\theta + \mathrm{DHI}_t \times f_{sky} + \mathrm{GHI}_t \times f_{ground} \tag{3}$$

$$\cos\theta = \cos Z \times \cos T + \sin Z \times \sin T \times \cos\left(\phi - \phi_p\right) \tag{4}$$

$$f_{sky} = \frac{1+\cos T}{2} \tag{5}$$

$$f_{ground} = \rho_{ground} \times \left(\frac{1-\cos T}{2}\right) \tag{6}$$

where $\cos\theta$ is the cosine of the angle between the PV panel's normal direction and the solar radiation direction, Z is the solar zenith angle, T is the PV panel tilt angle, ϕ is the solar azimuth angle, ϕ_p is the azimuth angle of the PV panel, f_{sky} is the correction factor for sky diffuse radiation, f_{ground} is the correction factor for ground-reflected radiation, and ρ_{ground} is the ground reflectance.

2.2.2. Wind turbine model

The maximum output power of the wind power system at time t, denoted as $p_{wind,t}$, is calculated as follows:

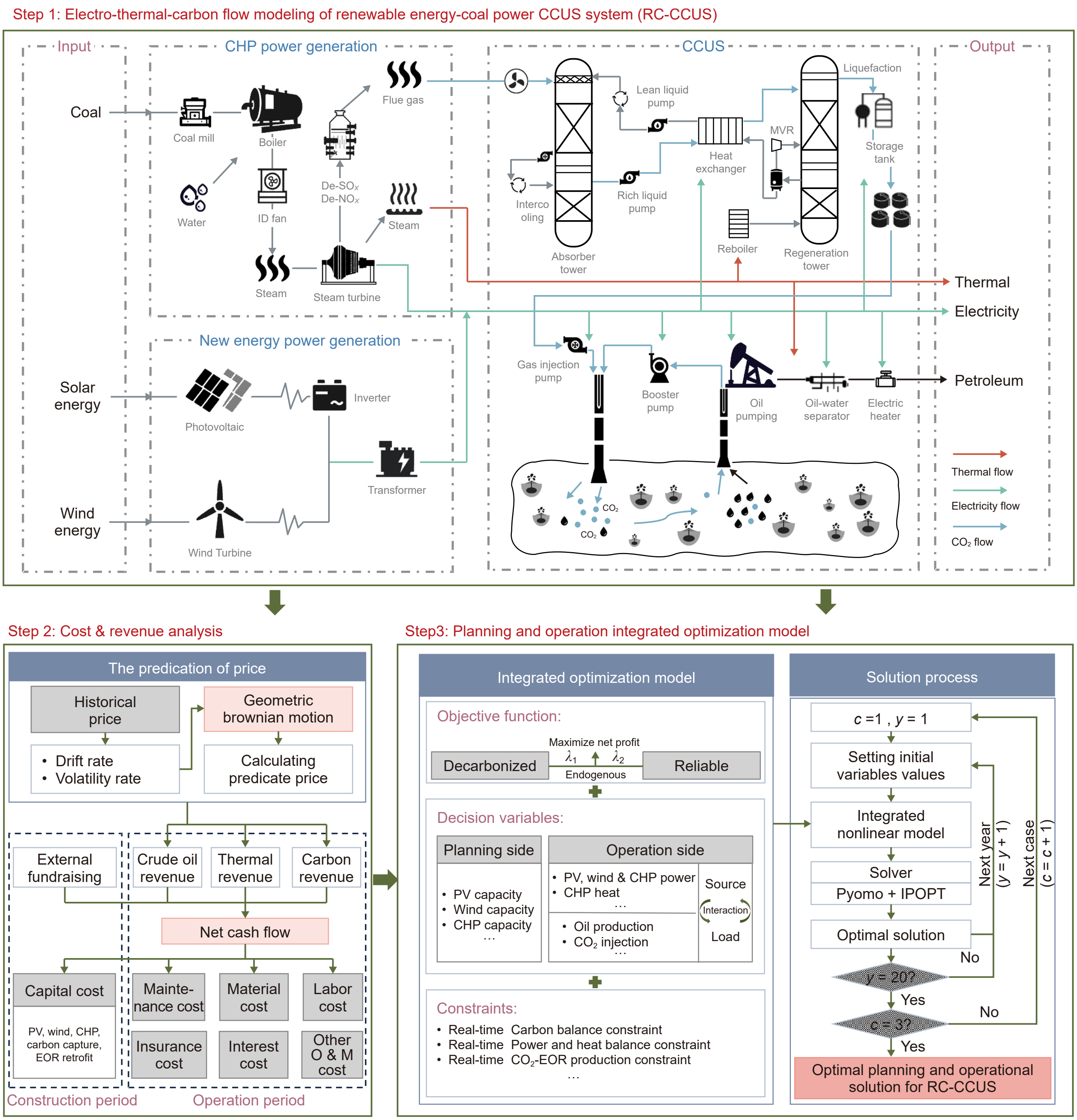

Fig. 1. Model framework.

$$p_{\text{wind},t} = p_{\text{rated},t} \times f_{\text{wind,system}} \tag{7}$$

where $p_{\text{rated},t}$ is the actual output power of the wind turbine at wind speed $v_{\text{wind},t,h}$, and $f_{\text{wind,system}}$ is the system correction factor. The calculation of $p_{\text{rated},t}$ is defined piecewise based on different wind speed ranges as follows:

$$p_{\text{rated},t} = \begin{cases} 0, v_{\text{wind}} < v_{\text{in}} \text{ or } v_{\text{wind}} \geq v_{\text{out}} \\ \left(\dfrac{v_{\text{wind},t,h} - v_{\text{in}}}{v_{\text{r}} - v_{\text{in}}}\right) \times c_{\text{rated}}, v_{\text{in}} < v_{\text{wind}} < v_{\text{r}} \\ c_{\text{rated}}, v_{\text{r}} < v_{\text{wind}} < v_{\text{out}} \end{cases} \tag{8}$$

where c_{rated} is the rated power of the wind turbine, v_{in}, v_r, and v_{out} represent the cut-in wind speed, rated wind speed, and cut-out wind speed, respectively, and $v_{wind,t,h}$ is the wind speed at height h.

To extrapolate the wind speed $v_{wind,t,h}$ from the reference height Z_{50m} to the turbine hub height $Z_{turbine}$, the calculations are performed using Eqs. (9) and (10).

$$v_{wind,t,h} = V_{50m}\left(\frac{Z_h}{Z_{50m}}\right)^{\alpha} \tag{9}$$

$$\alpha = \frac{\ln(V_{50m}) - \ln(V_{10m})}{\ln(Z_{50m}) - \ln(Z_{10m})} \tag{10}$$

where α is the wind shear exponent, V_{50m} and V_{10m} are the wind speeds at 50 m and 10 m above ground level, respectively, and Z_{50m} and Z_{10m} correspond to the reference heights of 50 m and 10 m, respectively.

2.2.3. CHP + CCS model

2.2.3.1. CHP model. The operation of the CHP system involves the simultaneous production of electricity and useful heat from a single energy source, improving overall energy efficiency. The core processes of the CHP system include the boiler superheater, initial electricity generation by the steam turbine, steam extraction for heating, and the reheater system. Under specified thermal and electrical load conditions, the electricity generation and heat supply of the cogeneration unit are determined as follows:

$$P_{chp} = E_{load} + E_{self-use} \tag{11}$$

$$Q_{chp} = \frac{Q_{mp} + Q_{lp}}{3.6} \tag{12}$$

$$P_{total} = P_{chp} + \eta_{turbine} \times Q_{coal} \tag{13}$$

$$E_{self-use} = P_{total} \times r_{self-use} \tag{14}$$

where P_{chp} is the total electricity generation, Q_{chp} is the total heat supply, and P_{total} corresponds to the total electricity generation of the cogeneration unit after equivalent thermal load adjustment. E_{load} is the electrical load, $E_{self-use}$ is the in-plant self-consumption of electricity, and Q_{mp} and Q_{lp} are the medium-pressure and low-pressure steam demands, respectively. $r_{self-use}$ is the self-consumption rate.

a. Steam cycle power generation process

a). Initial power generation by the steam turbine. The feed-water is heated by the boiler superheater to form high-temperature, high-pressure steam, which is then directed into the steam turbine for initial expansion and power generation.

$$E_{main} = Q_{sh} \times \eta_{boiler\ turbine} \times \eta_{turbine} \tag{15}$$

$$Q_{sh} = \Delta h_{main} * m_{main} \tag{16}$$

where E_{main} is the heat consumption for main steam power generation, Q_{sh} is the heat input to the superheater, $\eta_{boiler\ turbine}$ is the heat loss rate from the boiler to the turbine, and $\eta_{turbine}$ is the absolute internal efficiency of the turbine. Δh_{main} is the enthalpy increase of the main steam, m_{main} is the mass flow rate of steam produced by the boiler per hour.

b). Secondary power generation. Partially expanded steam is directed into the reheater system, where it is reheated to form reheated steam. The reheated steam is then returned to the steam turbine for secondary power generation.

$$E_{reh} = Q_{reh} \times \eta_{boiler\ turbine} \times \eta_{turbine} \tag{17}$$

$$Q_{reh} = \Delta h_{reh} \times m_{reh} \tag{18}$$

where E_{reh} is the heat consumption for reheated steam power generation, Q_{reh} is the heat value of the reheated steam, Δh_{reh} is the enthalpy increase of the reheated steam, m_{reh} is the mass flow rate of the reheated steam.

c). Leveraging the deep peak-shaving capability of the electric boiler, a combined heat supply method utilizing both the electric boiler and intermediate steam extraction is employed. In this approach, intermediate steam extraction is prioritized for heat supply, while the electric boiler provides supplementary heat.

$$Q_{coal} = Q_{st\ tap} + E_{dgl} \times \eta_{dr} \tag{19}$$

where $Q_{st\ tap}$ is the heat supply from intermediate steam extraction, E_{dgl} is the power consumption of the electric boiler, and η_{dr} is the electro-thermal conversion efficiency.

The cogeneration unit satisfies the following balance:

$$E_{coal} = (E_{main} + E_{reh}) \times 3.6 \tag{20}$$

$$m_{main} = m_{reh} + m_{mp} + m_{lp} \tag{21}$$

b. Water consumption calculation. The hourly water replenishment for CHP system is calculated as the steam flow rate at time t minus the recovered water volume at time $t-1$.

$$m_{water} = \max(0, m_{main}(t) - m_{reh}(t-1) \times (1 - \eta_r)) \tag{22}$$

where η_r is the condensation recovery rate.

c. Coal consumption and carbon emission calculation. Due to the nonlinear relationship between CHP load and standard coal consumption, the calculation method referenced from Lu et al. (2014) is adopted in this study:

$$m_{coal} = a \times {P_{total}}^2 + b \times P_{total} + c \tag{23}$$

$$m_{CO_2} = m_{coal} \times \mu_{carbon} \times \mu_{cc} \tag{24}$$

where m_{coal} is the standard coal consumption, and a, b, and c are the coal consumption coefficients of the unit, m_{CO_2} is CO_2 emissions, μ_{carbon} is the carbon content of standard coal, and μ_{cc} is the CO_2 conversion factor for standard coal.

2.2.3.2. Carbon capture model. The CO_2 capture system consists of two stages: capture and liquefaction. The capture stage typically uses chemical absorption with organic amine solutions (Rochelle, 2009). Flue gas is first pretreated in a composite absorption tower, where its temperature is reduced to −40 °C via alkaline washing, removing moisture, trace gypsum, and acidic gases to ensure optimal conditions for absorption. Absorbent regeneration involves removing impurities and dissolved organic compounds using activated carbon, followed by regeneration with low-pressure saturated/high-temperature steam, typically sourced from plant waste heat or auxiliary boilers (Liu et al., 2023). The energy and material consumption for both stages are calculated as follows:

a. Captured CO_2 quantity.

$$m_{CO_2\ cap} = m_{CO_2} \times \eta_{cap} \quad (25)$$

where $m_{CO_2\ cap}$ is the quantity of captured CO_2, m_{CO_2} is the CO_2 emissions from the CHP system and η_{cap} is the capture efficiency of the carbon capture system.

b. Total electricity consumption.

$$E_{cap} = m_{CO_2\ cap} \times e_{cap\ device} + m_{CO_2\ cap} \times e_{liq\ device} \quad (26)$$

The total electricity consumption E_{cap} is the sum of the electricity consumption in the capture stage and the liquefaction stage. $e_{cap\ device}$ and $e_{liq\ device}$ represent the unit electricity consumption for the capture stage and the liquefaction stage, respectively.

c. Total heat consumption.

$$Q_{cap} = m_{CO_2\ cap} \times h_{reb} \quad (27)$$

Q_{cap} is the regeneration heat consumption, which is the heat required for absorbent regeneration during the CO_2 capture process. h_{reb} is the regeneration heat consumption per unit of CO_2.

2.2.4. EOR model

CO_2-EOR uses captured CO_2 to enhance oil extraction in mature fields while storing CO_2 underground. Based on actual CO_2-EOR processes, the energy demands of four key stages—CO_2 injection, oil production, CO_2 reinjection, and gathering/transportation—are evaluated (Zhang et al., 2024). Energy consumption for each stage is calculated as follows:

$$E_{oilfield} = E_{inj} + E_{ext} + E_{reinj} \quad (28)$$

a. CO_2 injection stage. CO_2 is injected into the reservoir using high-pressure equipment (e.g., gas injection pumps, compressors) to boost formation pressure and enhance oil recovery. Electricity demand depends on the injection rate and equipment power.

$$E_{inj} = m_{CO_2\ inj} \times e_{inj} \quad (29)$$

where E_{inj} is the injection stage electricity consumption, $m_{CO_2\ inj}$ is the CO_2 injection rate (t/h), and e_{inj} is the electricity consumption per unit of injected CO_2.

b. Oil production stage. Key equipment includes pumping units and auxiliary heaters. Pumping units lift oil-containing fluids to the surface, with power demand tied to well depth, pump efficiency, and fluid production rate. Heaters prevent oil condensation and pipeline blockages. The fluid production rate for each well is calculated as follows:

$$m_{oil} = m_{liquid} \times n_{well} \times \frac{\alpha}{\alpha+1} \times (1 - \mathrm{water}_{cut}) \quad (30)$$

$$m_{liquid} = A_{tubing} \times L_{stroke} \times N_{strokes} \times 60 \times \varepsilon \times e_{pump} \quad (31)$$

$$A_{tubing} = \pi \times \left(\frac{d_{tubing}}{2}\right)^2 \quad (32)$$

where m_{oil} is the total oil production, water_{cut} is the water content, n_{well} is the total number of wells, and α is the ratio of production to injection wells. m_{liquid} is the fluid production rate per well, A_{tubing} is the tubing cross-sectional area, L_{stroke} is the stroke length, $N_{strokes}$ is the strokes per minute, ε is the pump efficiency, and e_{pump} is the pumping unit efficiency. The oil production stage energy consumption is calculated as follows:

$$E_{ext} = p_{pump\ unit} \times n_{well} \times \frac{\alpha}{\alpha+1} \quad (33)$$

$$p_{pump\ unit} = \left(p_{pump} + p_{heater} \times \epsilon + p_{aux}\right) \times e_{pump} \quad (34)$$

where E_{ext} is the total electricity consumption in the oil production stage, p_{pump}, p_{heater}, and p_{aux} are the power of the pumping unit, heater, and auxiliary equipment, respectively, and ϵ is a binary variable (1 for winter, 0 otherwise).

c. Reinjection stage. During CO_2-EOR, some CO_2 is recovered with produced fluids and reinjected into the reservoir using high-pressure compression and transport equipment.

$$E_{reinj} = m_{CO_2\ inj} \times \eta_{reinj} \times e_{reinj} \quad (35)$$

where E_{reinj} is the total electricity consumption during reinjection, η_{reinj} is the reinjection ratio, and e_{reinj} is the electricity consumption per unit of reinjected CO_2.

d. Gathering and transportation stage. This stage covers the transport, separation, and processing of oil-containing fluids from wells to treatment facilities, primarily involving oil-water separation and pipeline transport.

$$E_{ga-trans} = m_{oil} \times e_{sep} + m_{oil} \times e_{trans} \quad (36)$$

where e_{sep} is the electricity consumption per unit of oil-water treatment, and e_{trans} is the gas consumption per unit of oil transport.

2.2.5. Objective function

This study maximizes the oilfield production's annual total profit (TP_y). An oilfield IES planning and operational optimization model enables simultaneous optimization of equipment investment and hourly operations. A year-by-year optimization strategy ensures dynamic state transfer. The mathematical expressions are as follows:

$$\max TP_y = R_{oil,y} + R_{heat,y} + R_{carbon,y} - \sum_s C_{captial,s,y} - C_{O\&M,s,y} + \lambda_1 \sum_t^{8760} \left(p_{pv,t,y} + p_{wind,t,y}\right) - \lambda_2 \sum_t^{8760} \Delta p_{t,y} s \in \mathrm{pv,wind,chp,EOR} \quad (37)$$

where $C_{captial,s,y}$ and $C_{O\&M,s,y}$ are the capital and operational and maintenance (O&M) costs of system s in year y. $R_{oil,t}$, R_{heat} and $R_{carbon,y}$ are the revenue selling crude oil, high-pressure steam, and carbon market in year y. λ_1 is the decarbonization weight, with higher values indicating greater renewable energy generation. $p_{pv,t,y}$ and $p_{wind,t,y}$ are the power generation of PV and wind at time

t in year y. λ_2 is the stability weight, with higher values favoring self-consumption, it is assumed to be 0.025. $\Delta p_{t,y}$ is the power supply-demand imbalance at time t in year y.

In IES optimization, capital costs are a key factor in system economics. In year y, the capital cost of subsystem s is calculated as follows:

$$C_{\text{captial},s,y} = \sum_s \left(\sum_i C_{\text{eq},s,i,y} + C_{\text{con},s,y} + C_{\text{int},s,y} + C_{\text{tax},s,y} + C_{\text{other},s,y} \right) \times c_{s,y} \tag{38}$$

where $c_{s,y}$ is the installed capacity of subsystem s, and i is equipment within subsystem s. $C_{\text{eq},s,i,y}$ is the equipment acquisition cost, $C_{\text{con},s,y}$ is the construction and installation cost, $C_{\text{int},s,y}$ is the interest during construction, $C_{\text{tax},s,y}$ is the value-added tax, and $C_{\text{other},s,y}$ is other construction costs.

O&M costs are a critical factor influencing the long-term economics of the system. In year y, the O&M cost of subsystem s is calculated as follows:

$$C_{\text{O\&M},s,y} = \sum_s \left(\sum_j O_{\text{mat},s,j,y} + O_{\text{mai},s,y} + O_{\text{sal},s,y} + O_{\text{ins},s,y} + O_{\text{int},s,y} + O_{\text{other},s,y} \right) \times c_{s,y} \tag{39}$$

where j is raw materials in subsystem s production process. $O_{\text{mat},s,j,y}$ is cost of raw material j in subsystem s. $O_{\text{mai},s,y}$ is maintenance cost, $O_{\text{sal},s,y}$ is labor cost, $O_{\text{ins},s,y}$ is insurance cost, $O_{\text{int},s,y}$ is interest cost, and $O_{\text{other},s,y}$ is other O&M costs.

The system's revenue is calculated as follows:

$$R_{\text{oil},y} = \sum_{d=1}^{365} \left(\sum_{t \in \text{day}} m_{\text{oil},t} \times \text{price}_{\text{oil},d} \right) \tag{40}$$

$$R_{\text{heat},y} = \sum_{d=1}^{365} \left(\sum_{t \in \text{day}} Q_{\text{mp},t} \times \text{price}_{\text{heat},d} \right) \tag{41}$$

$$R_{\text{carbon},y} = \sum_{d=1}^{365} \left(\sum_{t \in \text{day}} m_{CO_2 \text{ pur},t} \times \text{price}_{\text{carbon},d} \right) \tag{42}$$

where $m_{\text{oil},t}$ is the oil production at hour t, $Q_{\text{mp},t}$ is the heat production at hour t, $m_{CO_2 \text{ pur},t}$ is the purchased CO_2 at hour t, $\text{price}_{\text{oil},d}$, $\text{price}_{\text{heat},d}$ and $\text{price}_{\text{carbon},d}$ are the oil price, heat price, and carbon price on day d, respectively.

2.2.6. Constrains

a. Real-time power generation constraints for PV and wind power. The real-time power generation of PV and wind power systems must not exceed the theoretical generation capacity under current weather conditions.

$$P_{\text{pv},t,y} \le p_{\text{pv},t,y} \times \sum_{k=1}^{y} \left(c_{\text{pv},k} - c_{\text{pv},k-1} \right) \times \prod_{\tau=k}^{y-1} \left(1 - \alpha_{\text{pv},\tau}\right) \tag{43}$$

$$P_{\text{wind},t,y} \le p_{\text{wind},t,y} \times \sum_{k=1}^{y} \left(c_{\text{wind},k} - c_{\text{wind},k-1} \right) \times \prod_{\tau=k}^{y-1} \left(1 - \alpha_{\text{wind},\tau}\right) \tag{44}$$

where $P_{\text{pv},t,y}$ and $P_{\text{wind},t,y}$ are the power generation of PV and wind at time t in year y. $c_{\text{pv},y}$ and $c_{\text{wind},y}$ are the installed capacities of PV and wind in year y. $\alpha_{\text{pv},y}$ and $\alpha_{\text{wind},y}$ are the annual degradation rates of PV modules and wind turbines in year τ.

b. Power and heat balance constraints. CHP power supply must exceed the power deficit, and heat supply must meet the heat load to ensure power and heat balance.

$$P_{\text{chp},t} - E_{\text{self use},t} \ge \max\left(E_{\text{cap},t} + E_{\text{oilfield},t} - P_{\text{pv},t} - P_{\text{wind},t}, 0 \right) \tag{45}$$

$$E_{\text{self use},t} = \left(E_{\text{cap},t} + E_{\text{oilfield},t} + \eta_{\text{turbine}} \times Q_{\text{cap},t} \right) * r_{\text{self-use}} \tag{46}$$

$$Q_{\text{chp},t} \ge Q_{\text{mp},t} + Q_{\text{cap},t} \tag{47}$$

where $P_{\text{chp},t}$ is the total CHP power supply at time t, $E_{\text{self-use},t}$ is the self-consumption at time t, and $Q_{\text{chp},t}$ is the heat supply at time t.

c. Carbon balance constraint.

$$\sum_{t \in T} m_{CO_2 \text{ inj},t} + \sum_{t \in T} m_{CO_2 \text{ to air},t} = \sum_{t \in T} m_{CO_2 \text{ pur},t} + \sum_{t \in T} m_{CO_2 \text{ cap},t} \tag{48}$$

where $m_{CO_2,t}$ and $m_{CO_2 \text{ cap},t}$ are the total carbon emissions and captured carbon from the CHP unit at time t, respectively. $m_{CO_2 \text{ inj},t}$ is the CO_2 injection for EOR at time t, $m_{CO_2 \text{ to air},t}$ is the CO_2 emitted to the air, and $m_{CO_2 \text{ pur},t}$ is the CO_2 purchased from external sources.

d. CO_2 storage tank constraints. The hourly storage change is calculated based on the balance of capture, purchase, injection, and storage. The CO_2 storage must not exceed the tank's capacity.

$$m_{CO_2 \text{ sto},t} = \begin{cases} m_{CO_2 \text{ pur},t} + m_{CO_2 \text{ cap},t} - m_{CO_2 \text{ inj},t}, t = 0 \\ m_{CO_2 \text{ sto},t-1} - m_{CO_2 \text{ pur},t} + m_{CO_2 \text{ cap},t} - m_{CO_2 \text{ inj},t}, t > 0 \end{cases} \tag{49}$$

where $m_{CO_2 \text{ sto},t}$ is the storage amount in the tank at time t.

e. CO_2-EOR production constraints. Annual oil production is capped at the target level, with daily production meeting minimum requirements. CO_2 injection is limited to a range tied to annual oil output.

$$\sum_{t \in T} m_{\text{oil},t} = p_{\text{oil}} \tag{50}$$

$$\sum_{t \in [1,24]} m_{\text{oil},t} \ge p_{\text{oil daily}}, \forall d \in \{1, 2, \cdots, 365\} \tag{51}$$

$$\sum_{t \in T} m_{CO_2 \text{ inj},t} \in \left[p_{\text{oil}} \times r_{CO_2-\text{oil}}, p_{\text{oil}} \times r_{CO_2-\text{oil}} \times 1.2 \right] \tag{52}$$

where p_{oil} is the annual oil production target, $p_{oil\ daily}$ is the minimum daily production, and r_{CO_2-oil} is the annual CO_2-oil replacement rate.

f. Ramp rate constraints for CHP.

$$r_{min\ ramp} \le \frac{P_{coal,t} - P_{coal,t-1}}{\Delta t} \le r_{max\ ramp} \tag{53}$$

where $P_{coal,t}$ is the coal-fired CHP power output at time t, Δt denotes the time interval, and $r_{min\,ramp}$ and $r_{max\,ramp}$ are the lower and upper ramping limits of the CHP unit, respectively.

g. Other fluctuation constraints.

$$\left|\frac{e_{pump,t} - e_{pump,t-1}}{\Delta t}\right| \le r_{max\ pump} \tag{54}$$

$$\left|\frac{m_{CO_2\ inj,t} - m_{CO_2\ inj,t-1}}{\Delta t}\right| \le r_{max\ inj} \tag{55}$$

where e_{pump} is the pumping unit efficiency. $r_{max\ pump}$ and $r_{max\ inj}$ are the maximum fluctuation rates for pumping efficiency and CO_2 injection rate.

h. Capacity and boundary constraints.

$$c_{sto\ tank} \ge \max\left(m_{CO_2\ storage,t}\right) \tag{56}$$

$$c_{capture} \ge \sum_{t \in T} m_{CO_2,t} \tag{57}$$

$$0 \le m_{CO_2\ pur,t} \le \max_{CO_2\ pur} \tag{58}$$

$$0 \le m_{CO_2\ inj,t} \le \max_{CO_2\ inj} \tag{59}$$

where $\max_{CO_2\ pur}$ is the maximum hourly CO_2 purchase limit, and $\max_{CO_2\ inj}$ is the maximum hourly CO_2 injection limit.

i. Installed capacity expansion constraints. Current installed capacity must not be less than the previous period's capacity to enable expansion.

$$c_s^y \ge c_s^{y-1} \tag{60}$$

In addition, renewable energy capacity is subject to spatial constraints imposed by the available land area within the oilfield:

$$c_{pv}^y * a_{pv} + c_{wind}^y * a_{wind} \le A_{oilfield} \tag{61}$$

where a_{pv} represents the land area required per unit of PV capacity, a_{wind} represents the land area required per unit of wind capacity, and $A_{oilfield}$ denotes the total available land area for renewable energy deployment in the oilfield.

2.2.7. Indicator evaluation

This study further conducts a comprehensive quantitative evaluation of the optimization results in terms of economic, decarbonization, and reliability.

a. Economic indicator. σ_{npv} measures the system's economic performance over the planning period using net present value (NPV):

$$\sigma_{npv} = \sum_{y}^{20} \frac{CF_y}{(1+r)^y} - \sum_{s} C_{captial,s,y} \tag{62}$$

where CF_y is the net cash flow in year y, and r is the discount rate.

b. Decarbonization indicator. σ_{re} reflects the system's low-carbon performance as the annual average renewable energy generation share:

$$\sigma_{re} = \frac{1}{20} \sum_{y}^{20} \frac{\sum_{t}^{8760} \left(p_{pv,t,y} + p_{wind,t,y}\right)}{\sum_{t}^{8760} p_{total,t,y}} \times 100\% \tag{63}$$

where $p_{total,t,y}$ is the total power generation at time t in year y.

c. Reliability indicator. σ_{ld} assesses supply-demand balance by calculating the dynamic normalized fluctuation rate (Khan and Javaid, 2020). A lower value indicates better source-load interaction:

$$\sigma_{ld} = \frac{1}{20} \sum_{y=1}^{20} \sigma_{ld,y} = \frac{\sum_{t}^{8760} \left|\Delta p_{t,y}\right|}{8760 * L_{avy,y}} \tag{64}$$

where $\Delta p_{t,y}$ is supply and demand power deviation, $L_{avy,y}$ is the average load in year y.

3. Data

The hourly PV and wind energy resources for a certain region in Xinjiang, China, in 2023 are presented in Fig. 2. This study utilizes Monte Carlo simulations to model the uncertainties associated with solar radiation, wind speed and price. The historical prices of coal, crude oil, industrial CO_2, carbon and time-of-use electricity

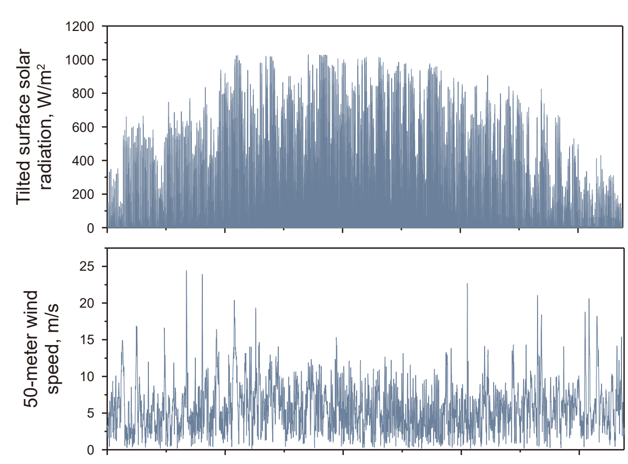

Fig. 2. Irradiance and wind speed in Xinjiang, China in 2023.

Table 2
Key technical parameters of the RC-CCUS.

Equipment	Parameter	Parameter description	Value
PV	η_{module}	Module conversion efficiency	22.50%
	$f_{pv,system}$	Loss factor	87.23%
	p_{module}	Module power capacity	580 W
	A_{panel}	Module surface area	2.583 m^2
	T	Solar tilt angle	38°
	a_{pv}	Land area required of PV capacity	202.47 m^2/kW
Wind	$f_{wind,system}$	System correction factor	80%
	v_{in}	Cut-in wind speed	3 m/s
	v_r	Rated wind speed	11.3 m/s
	v_{out}	Cut-out wind speed	25 m/s
	Z_h	Turbine hub height	110 m
	a_{wind}	Land area required of wind capacity	71.20 m^2/kW
CHP	a, b, c	–	7.2E-05, 0.23, 14.62
	η_{boiler}	Boiler efficiency	92.67%
	$\eta_{turbine}$	Turbine efficiency	43.84%
	$r_{self\ use}$	Self-use power ratio	6%
	$\eta_{boiler\ to\ turbine}$	Boiler to turbine efficiency	83.03%
	μ_{carbon}	Standard coal carbon content	71%
	μ_{cc}	Standard coal CO_2 conversion factor	3.67 t/t
	$r_{max\ ramp}$	Maximum ramp rate	12 MW/min
CCS	η_{cap}	Capture efficiency	90%
	h_{reb}	Heat requirement for reboiler	2.4 GJ/t CO_2
	$e_{cap\ device}$	Electricity consumption of capture CO_2	51.04 KWh/t CO_2
	$e_{liq\ device}$	Electricity consumption of liquefaction CO_2	170.13 KWh/t CO_2
EOR	$water_{cut}$	Water cut	80%
	η_{reinj}	Reinjection ratio	23%
	p_{pump}	Pump power	55 kW
	p_{heater}	Heater power	20 kW
	p_{aux}	Auxiliary power	2 kW
	L_{stroke}	Stroke length	2.5 m
	$N_{strokes}$	Strokes per minute	8 strokes/min
	A_{tubing}	Tubing cross-sectional area	0.05 m^2
	e_{inj}	Electricity consumption of injected CO_2	54.99 KWh/t oil
	e_{reinj}	Electricity consumption of reinjected CO_2	54.99 KWh/t oil
	e_{sep}	Electricity consumption of oil-water treatment	39.89 KWh/t oil
	e_{trans}	Gas consumption of oil transport	51.04 m^2/t oil
	$A_{oilfield}$	Total available land area	106 km^2

are collected from Wind and Bloomberg database. The key technical parameters of the IES are provided in Table 2.

To validate the effectiveness of the refined energy equipment modeling and the integrated planning-operation optimization method, three cases with distinct energy-technology configurations were designed: Case 1 (Renewable energy + CHP + CCUS + Source-load interaction), Case 2 (Renewable energy + CHP + CCUS + Stable production), and Case 3 (Grid + CCUS + Stable production). Cases 2 and 3 were used as baseline comparisons to assess the model's generalizability under different operational constraints and technology mixes.

4. Results and discussion

4.1. Oilfield IES planning and operational optimization results

Oilfield development follows a two-phase pattern. In the ramp-up phase (1st–12th years), crude oil output increases at 0.12 Mt per year, peaking at 2.33 Mt in 12th year, while CO_2 injection rises from 3.13 to 7.26 Mt to support enhanced oil recovery. In the stable production phase (13th–20th year), CO_2 injection maintains an output of 2.30 Mt per year.

Fig. 3 compares the planning results of the oilfield IES under two different production modes. In Case 1, as the oilfield production capacity expands, PV capacity increases significantly by 215%–392 MW, wind power capacity rises by 94%–301 MW, CHP capacity increases by 88%–593 MW, while carbon capture capacity also increases by 73% to 3.9 Mt. In contrast, Case 2, which operates under a stable load production mode, exhibits distinctly different

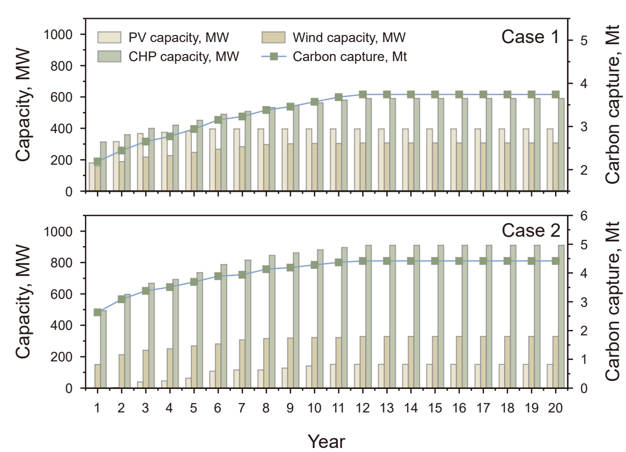

Fig. 3. Installed capacities of PV, wind power, CHP, and carbon capture infrastructure over the planning period.

characteristics. The system relies heavily on larger clean coal units and carbon capture facilities to ensure the security and cleanliness of the energy supply. In the stable production phase, CHP capacity increases by 84%–910 MW. Simultaneously, the system requires higher carbon capture capacity to minimize its environmental impact, with carbon capture rising to 4.4 Mt. However, the development of renewable energy is severely constrained, with PV capacity only reaching 152 MW, while wind power capacity slightly increases to 330 MW.

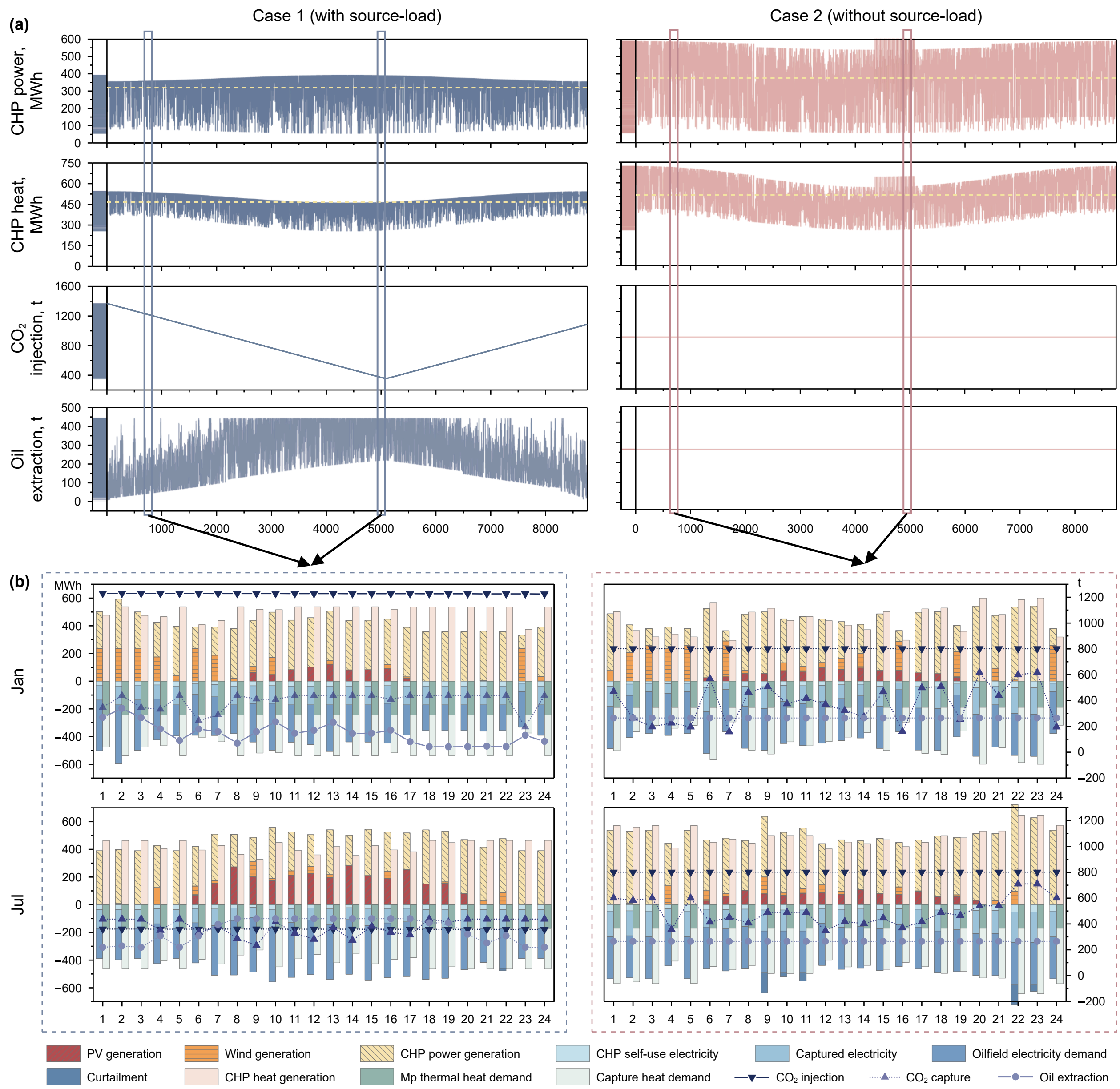

Fig. 4. Comparison of CHP power, heat, CO_2 injection, and oil extraction between Case 1 and Case 2 in 20th year.

In the oilfield IES, flexible loads are classified into two categories. Electrical flexible loads (e.g., electric submersible pumps, progressing cavity pumps, CO_2 compression, CO_2 injection and electric heating) can be regulated hourly through frequency control, staggered start-stop, and well group rotation. Quasi-flexible thermal loads, such as solvent circulation and regeneration in CO_2 capture and pipeline insulation, are bound by heat balance, fluid quality, minimum transport temperature, and safety constraints, permitting only limited intra-band adjustment. Fig. 4 illustrates the optimized real-time operation results for representative winter and summer days derived from the proposed framework.

In winter, Case 2 maintains a fixed EOR output and a nearly constant electricity load (314.43 MW), resulting in minimal alignment with wind–solar fluctuations. System variability is largely absorbed by the CHP, which ramps at 117.3 MW/h, while coal-fired and industrial heating remain rigid. In contrast, Case 1 adopts flexible scheduling (daytime extraction, nighttime recovery, well-group rotation, tiered power allocation), reducing average load to 267.17 MW and improving correlation with renewables to 0.866. CHP ramping falls to 59.03 MW/h, and daytime well productivity increases by 60%. Seasonal contrasts are magnified in summer. Case 2 sustains a nearly constant 303.39 MW load with only 14.26% renewable penetration and

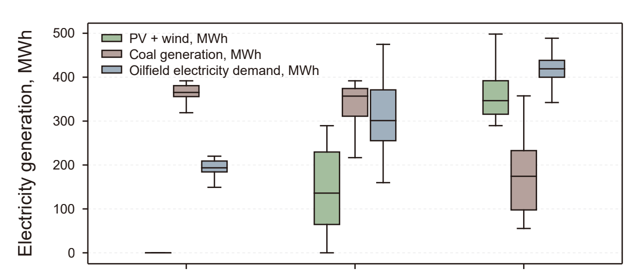

Fig. 5. Distribution of PV + wind and coal generation relative to demand across low-RES, non-extreme, and high-RES hours under Case 1.

69.72 MW/h CHP ramping. Case 1, by following renewable availability, raises average load to 323.72 MW, increases renewable penetration to 30.41%, and achieves a correlation of 0.959. CHP ramping remains controlled at 123.35 MW/h, and daytime productivity is 73.9% higher than nighttime. These results highlight the efficiency and low-carbon benefits of flexible source-load coordination.

Carbon-energy interactions are shaped jointly by seasonal supply-demand patterns and operational flexibility. In winter, higher CHP output ensures abundant CO_2 supply, with the average injection rate reaching 1222.97 t/h. In summer, maintenance outages and partial-load operation reduce CO_2 availability, while intensified industrial demand raises CO_2 prices by 21.46% compared to winter. Accordingly, a seasonally differentiated EOR injection strategy is adopted: injection is maximized in winter and

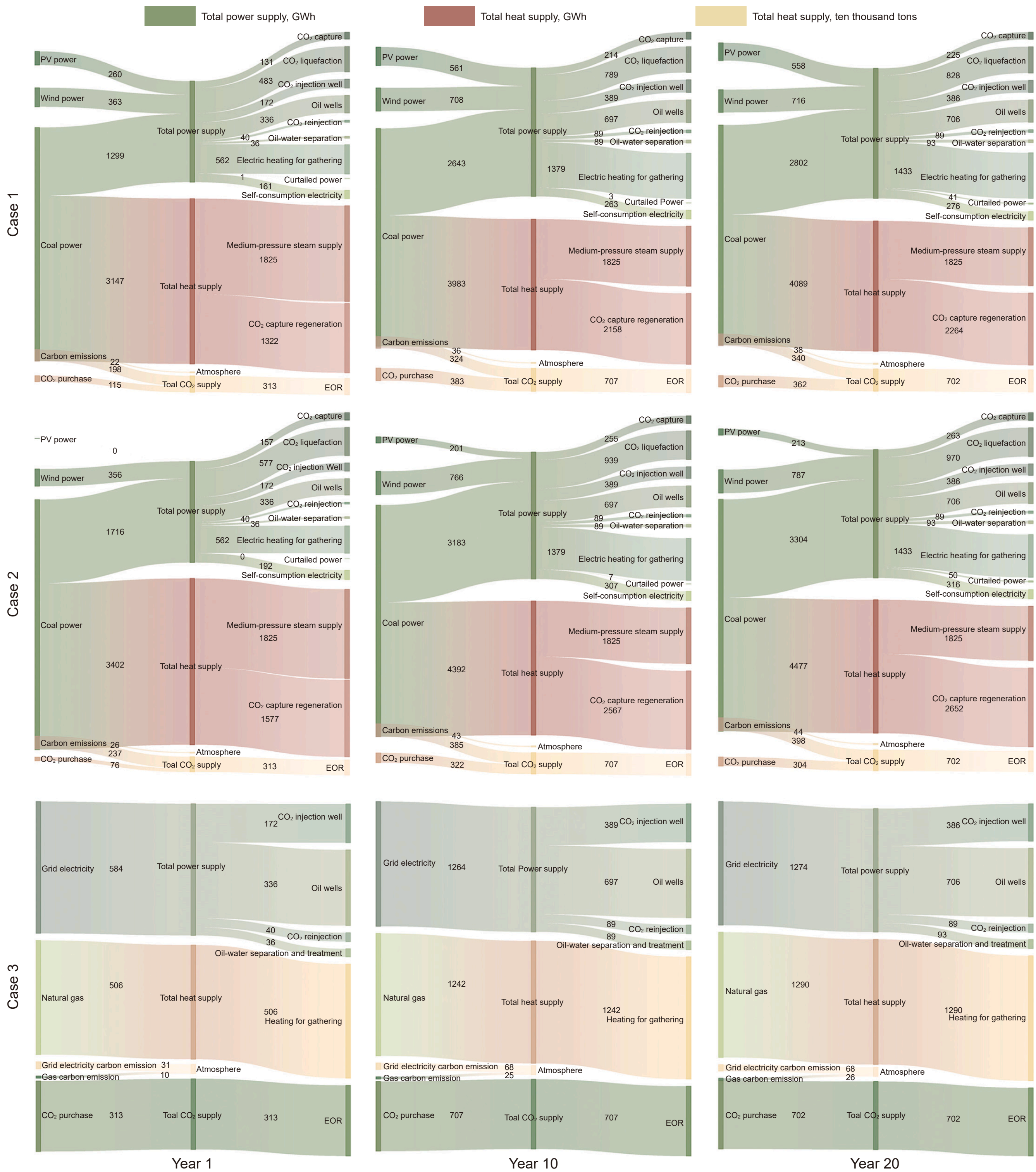

Fig. 6. Electricity, heat, and carbon flow dynamics in the 1st, 10th, and 20th years of the planning period.

moderated in summer (average 360.57 t/h), which both tracks market signals and releases electro-thermal capacity to support flexible production under renewable variability.

As shown in Fig. 5, under the Case 1 configuration, the hourly operating states are classified into low renewable energy supply (low-RES), non-extreme renewable supply (non-extreme), and high renewable energy supply (high-RES) conditions (905/6979/876 h, respectively). During High-RES periods, PV and wind generation increases substantially (357.7 MWh), enabling the oilfield to raise electricity demand to 413.5 MWh while suppressing coal-fired output to 173.0 MWh. Conversely, under Low-RES conditions, renewable supply is nearly absent, prompting the system to reduce electricity demand to 195.2 MWh and increase coal-fired generation to 365.2 MWh to maintain heat-power security. The Non-Extreme regime shows intermediate behavior (PV + wind 139.3 MWh, demand 310.6 MWh, coal 327.6 MWh). These results demonstrate a clear renewable-contingent operational strategy: when renewable availability is high, the system shifts to load absorption and coal displacement; when it is low, demand is curtailed and coal generation becomes the primary stabilizing resource to ensure continuous supply.

Fig. 6 illustrates the system's energy and material flow characteristics in the 1st, 10th, and 20th years. In Case 3, the system relies entirely on the external power grid for electricity supply, while heat is provided through natural gas combustion. Total electricity demand increases from 584 GWh in 1st year to 1274 GWh in 20th year, with consumption primarily concentrated in energy-intensive processes such as oil well recovery (56.0%), CO_2 injection (30.2%), CO_2 reinjection (6.9%), and oil-water separation (6.9%). Heat demand is mainly associated with gathering and transmission heating. CO_2 supply is fully dependent on external procurement, with annual purchases rising from 3.13 to 7.07 Mt, underscoring the system's lack of self-regulation and long-term sustainability. Under this scenario, the CO_2-EOR process exhibits a carbon intensity of 456.4 $kgCO_2$ per ton of oil, with annual emissions reaching 0.94 Mt during the stable production stage.

With the introduction of the IES in Case 2, the CHP system emerges as the central hub for coordinated electricity, heat, and carbon supply, while the share of renewables increases to 23.2%. Electricity use follows a clear hierarchy in which gathering and transmission heating accounts for 33.3%, carbon liquefaction 22.5%, and CO_2 injection wells 16.4%, together representing more than 70% of total demand. In comparison, CHP self-consumption, carbon capture, and CO_2 reinjection together contribute less than 20%. On the heat side, solvent regeneration in amine-based carbon capture dominates, supplemented by medium-pressure steam extraction for industrial waste heat recovery. Expansion of coal-fired generation raises captured CO_2 from 2.4 to 4.0 Mt, yet internal supply meets only 48% of the EOR injection demand, driving external procurement from 0.76 to 3.0 Mt. Residual emissions mainly stem from uncaptured CO_2, totaling 0.442 Mt annually during stable production, which represents a substantial reduction relative to Case 3.

The optimized Case 1 system with source-load interaction markedly improves renewable integration. While the CHP system remains the dominant energy source, wind and PV penetration increases modestly from 31.3% to 32.4%. At the same time, the CHP heat-to-power ratio falls from 2.42 to 1.46, indicating a transition from a heat-driven model to an electricity-heat synergistic model, marking a significant step in energy structure optimization. Compared with Case 2, where the ratio declines from 1.98 to 1.35, Case 1 delivers a more substantial structural shift while still maintaining a high ratio to satisfy the heat demand of carbon capture. In terms of carbon emissions, the internal CO_2 supply in Case 1 meets only 56% of the requirement for EOR injection, and external procurement rises from 1.2 to 3.8 Mt over the 20-year horizon.

4.2. Economic and multi-indicator analysis results across cases

The economic performance of the oilfield IES across the three cases (Fig. 7) reveals significant differences. Case 1 demonstrates the highest NPV of 36.52 billion CNY at a 6% discount rate, surpassing Case 2 by 10.26% and Case 3 by 11.61%, reflecting its superior economic efficiency. This outcome is driven by dynamic supply-demand matching, which maximizes renewable energy utilization through load shifting and strengthens CHP load-following flexibility. As a result, total installed capacity is reduced, capital expenditure falls by 1.22 billion CNY, and operational efficiency improves. Annual CHP operating hours increase from 3631 to 4726 h, yielding 1.34 billion CNY in fuel and operational savings compared with Case 2. Case 2 performs moderately well but lacks the full benefits of flexible coordination, while Case

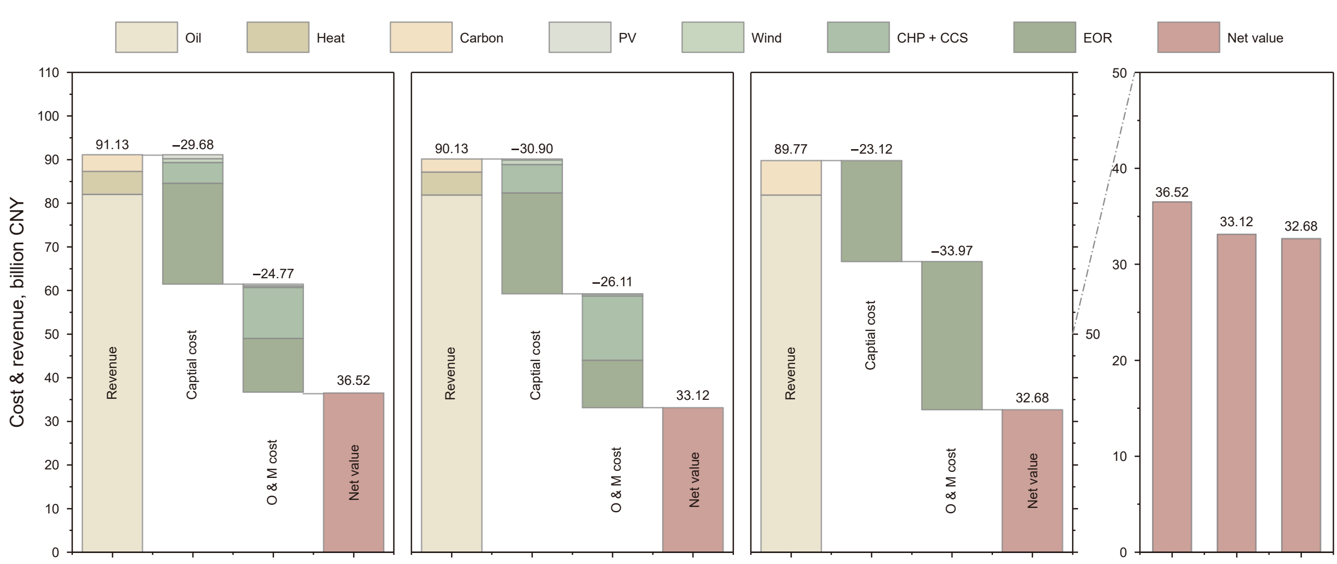

Fig. 7. Cost-benefit comparison across Case 1, Case 2, and Case 3.

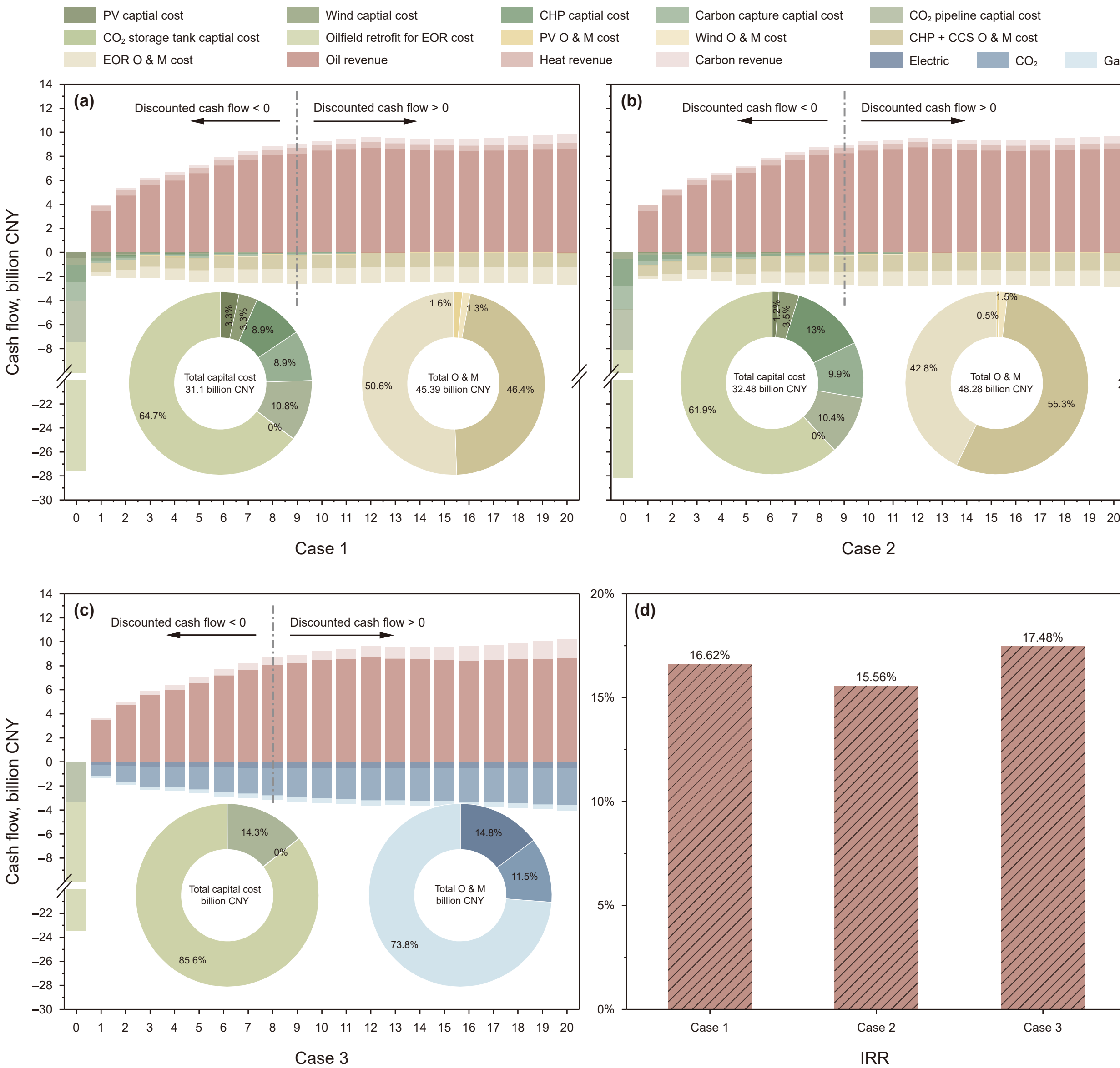

Fig. 8. **(a)**–**(c)** Annual cash flow dynamics of the RC-CCUS system for Cases 1, 2, and 3; **(d)** Internal rate of return (IRR) evaluation for Cases 1, 2, and 3.

3, without renewables or CCUS, faces the heaviest economic burden, with operational costs reaching 33.97 billion CNY due to high dependence on purchased electricity and external CO_2 procurement.

The comparative analysis of cash flow dynamics, shown in Fig. 8, highlights clear differences in investment structures and operating costs. Case 1 delivers the strongest economic performance, with total capital expenditure of 31.1 billion CNY. Most of the investment is directed to oilfield EOR retrofitting, which accounts for 64.7%, and to carbon infrastructure, which accounts for 19.7%, while renewables and CHP together contribute 15.5%. This allocation ensures stable operating costs in the mature phase between 10th and 20th year, with renewable O&M expenses remaining steady at 32–40 million CNY for PV and 28–37 million CNY for wind, whereas fossil-based system costs gradually rise from 1.08 to 1.17 billion CNY. Case 2 requires a higher fixed asset investment of 32.5 billion CNY, 4.5% more than Case 1, largely due to greater allocations for CHP and CCS infrastructure. The expanded CHP and CCS capacity raises annual O&M costs to 1.40–1.49 billion CNY. However, the enhanced capture capacity reduces reliance on purchased CO_2, lowering EOR O&M costs to 1.15–1.35 billion CNY. Case 3 requires substantially lower capital investment—23.49 billion CNY, representing a 24.5% reduction relative to Case 1—with 85.6% allocated to oilfield retrofitting. However, this cost-saving strategy results in considerably higher operating expenditures, driven by annual electricity costs of 0.52–0.53 billion CNY, natural gas costs of 0.41–0.42 billion CNY, and CO_2 procurement costs of 2.50–3.10 billion CNY. Across all cases, carbon trading revenues help to offset the decline in oil revenues. Case 1 achieves the greatest benefit, with carbon revenues rising from 4.45% to 8.59% of total income as carbon prices increase from 417 to 853 CNY per ton. District heating contributions remain steady at 4.62%, ensuring robust annual revenues of 9.3–9.9 billion CNY throughout the mature operational phase.

As shown in Fig. 8(d), the relatively lower IRR of Case 2 compared with Case 3 arises from its larger-scale integration of renewables and higher upfront capital investment, which delay the break-even point and weaken early cash flow performance.

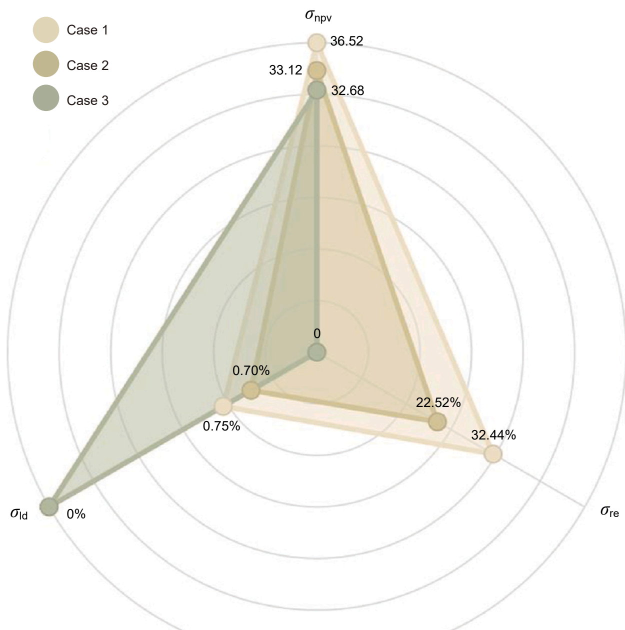

Fig. 9. Three-dimensional evaluations of economic, stability, and low-carbon performance across Case 1, Case 2, and Case 3.

Yet the 20-year horizon does not fully capture Case 2's long-term technical advantages, as the extended lifespans of its assets—30 years for CHP and 25 years for PV and wind—together with declining marginal costs are expected to deliver sustained benefits beyond the assessment period. By contrast, Case 3's profitability is highly vulnerable to market volatility, particularly in electricity procurement and CO_2 sourcing. Case 1, which secures a higher IRR than Case 2 while remaining broadly comparable to Case 3, demonstrates superior efficiency across both short- and long-term horizons, underscoring the resilience and structural flexibility conferred by an integrated energy system.

In the reliability dimension (Fig. 9), the combination of source-load interaction and real-time optimization deliver clear advantages. Case 1 achieves a load deviation (σ_{ld}) of 0.70%, a 6.67% improvement over Case 2 at 0.75%. As shown in Fig. 4, the load fluctuation of CHP units in Case 1 is reduced by 41.4% relative to Case 2, lowering regulation costs and mitigating equipment aging from frequent ramping, thereby enhancing long-term stability. Although Case 3 theoretically achieves $\sigma_{ld} = 0$ by relying on grid regulation, this shifts the burden to the external grid, increasing regional dispatch pressure and systemic risk. On the decarbonization front, Case 1 also holds a significant advantage, achieving a renewable penetration of 32.44%.

4.3. Multi-objective sensitivity analysis

To assess the influence of decarbonization and reliability priorities in Case 1, the decarbonization weight λ_1 and reliability weight λ_2 were set to {0, 0.05, 0.10} and {0, 0.025, 0.05}, corresponding to lenient, moderate, and strict constraint intensities. As shown in Fig. 10, increasing the decarbonization preference under moderate reliability ($\lambda_2 = 0.025$) leads to a marked expansion of renewable capacity during the stable production period, with wind and PV capacities rising from 301/392 to 667/776 MW. Conversely, tightening the reliability constraint under moderate

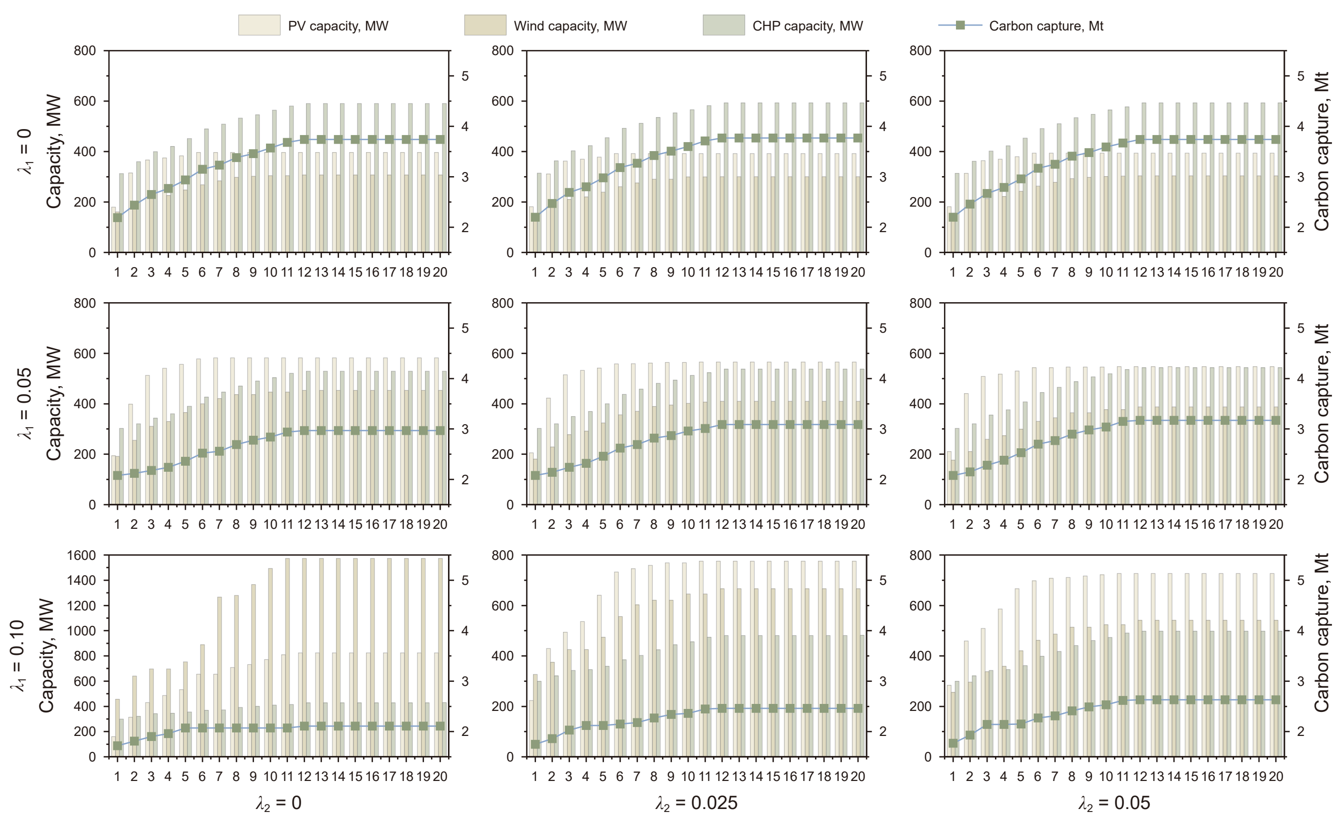

Fig. 10. Installed capacity mix under different weight parameters.

Table 3
Trade-offs among economic, decarbonization, and reliability under different weighting preferences.

Parameters			Indicator	Economic (σ_{npv})	Decarbonization (σ_{re}), %	Reliability (σ_{ld}), %
λ_1	0	λ_2	0	35.74	33.20	0.87
			0.025	36.52	32.44	0.70
			0.05	35.71	32.88	0.65
	0.05	λ_2	0	35.75	49.44	5.12
			0.025	35.79	46.48	3.51
			0.05	35.79	44.38	2.68
	0.01	λ_2	0	32.91	78.08	58.21
			0.025	35.06	63.52	16.07
			0.05	35.49	58.20	9.82

decarbonization preference ($\lambda_1 = 0.05$) shifts the capacity mix from (582 MW wind + 453 MW PV) with 530 MW coal to (548 MW wind + 388 MW PV) with 544 MW coal, reflecting a structural shift toward dispatchable power.

The performance results in Table 3 indicate a clear operating threshold. When the wind-solar share is maintained at around 50%, the system attains a balanced regime: economic returns remain stable ($\sigma_{npv} \approx 35.5$–35.8 billion CNY) and reliability stress is contained ($\sigma_{ld} \approx 3\%$–5%), while decarbonization remains effective. Beyond this range, further emissions reduction is achieved mainly through continued capacity expansion, which triggers a non-linear increase in operational stress (σ_{ld} up to 58.21%) and a decline in economic performance. The system thereby shifts into a high-cost operating state. These results suggest that maintaining a renewable share near ~50% yields the most favorable trade-off among decarbonization outcomes, economic viability, and reliability.

5. Conclusions

By using the planning-operation integrated optimization model, the installed capacity of the oilfield IES is obtained for producing 2.30 Mt crude oil per year. The Case 1 is equipped with 593 MW CHP, 301 MW wind, 392 MW PV, and 3.74 Mt CCS capacity, on the other hand, The Case 2 requires 910 MW CHP, 330 MW wind, 152 MW PV, and 4.40 Mt CCS.

The oilfield IES increases NPV by 10.26% and 1.35% in Case 1 and Case 2 comparing with Case 3 respectively, supporting a cost-effective transition. At the same time, all three scenarios realize negative-carbon operation, and the net emission reductions of Case 1 and Case 2 are 9.20% and 8.20% higher respectively comparing with Case 3. Therefore, the findings reveal that the economic and decarbonization benefits in Case 1 and Case 2 are improved substantial with a very limited reduction of reliability degree comparing with Case 3, and it offers an efficient solution to the trilemma in the low-carbon transition in oilfield energy system.

The Case 1 with source-load interaction improves the performance in economic, decarbonization and reliability by 9.04%, 1.00% and 6.67% respectively compared to the Case 2. These improvements are attributable to the coordinated scheduling of flexible oilfield load, including electric submersible pumps, progressing cavity pumps, CO_2 compression and injection, and electric heating using strategies such as daytime extraction with nighttime recovery, well-group rotation, and tiered power allocation.

6. Limitations and future work

This study focuses on a representative oilfield system and does not yet extend to larger regional or national-scale comparative analysis. In addition, the model adopts deterministic parameters and does not account for uncertainties such as price volatility and technological progress. Future work may expand the analysis to interconnected multi-regional systems and incorporate stochastic optimization or real-options approaches to evaluate investment and operational decisions under uncertainty, while also including additional low-carbon technologies such as energy storage and hydrogen to enhance the model's applicability.

CRediT authorship contribution statement

Zhi-Hui Gao: Writing – original draft, Software, Methodology, Investigation, Data curation. **Ding-Ding Wang:** Visualization, Validation, Methodology, Investigation, Data curation. **Jiang-Feng Liu:** Writing – review & editing, Supervision, Methodology. **Shao-Jie Hao:** Visualization, Validation, Investigation, Data curation. **Qi Zhang:** Writing – review & editing, Supervision, Conceptualization.

Declaration of competing interest

The authors declare that they have no known competing financial interests or personal relationships that could have appeared to influence the work reported in this paper.

Acknowledgements

The authors gratefully acknowledge the support provided by Central Guidance on Local Science and Technology Development Fund (ZYYD2025ZY13) and National Social Science Foundation of China (No.24VRC022).

Abbreviations

NC-IES	Negative carbon integrated energy systems
CHP	Combined heat and power
EOR	Enhanced oil recovery
GHG	Greenhouse gas
DNI	Direct normal irradiance
GHI	Global horizontal irradiance
IES	Integrated energy systems
CCUS	Carbon capture, utilization, and storage
NPV	Net present value
RC-CCUS	Renewable energy-CHP-CCUS
DHI	Diffuse horizontal irradiance
CO_2	Carbon dioxide

References

An, K., Zheng, X., Shen, J., et al., 2025. Repositioning coal power to accelerate net-zero transition of China's power system. Nat. Commun. 16, 2311. https://doi.org/10.1038/s41467-025-57559-2.

Ao, X., Zhang, J., Yan, R., et al., 2025. More flexibility and waste heat recovery of a combined heat and power system for renewable consumption and higher efficiency. Energy 315, 134392. https://doi.org/10.1016/j.energy.2025.134392.

Cao, Y., Song, M.H., Zhao, W.D., et al., 2020. Analysis on energy efficiency evaluation method of key energy system in oil and gas fields: taking the Tarim oilfield as an example. Chem. Eng. Oil Gas 49 (3), 106–114. https://doi.org/10.3969/j.issn.1007-3426.2020.03.018 (in Chinese).

Chai, T., Li, M., Zhou, Z., et al., 2023. An intelligent control method for the low-carbon operation of energy-intensive equipment. Engineering 27, 84–95. https://doi.org/10.1016/j.eng.2023.05.018.

CNPC, 2022. The First New Energy Photovoltaic Power Generation Demonstration Base of North China Oilfield Commences Operations. https://www.cnpc.com.cn/cnpc/xgdt/202205/d1e7361df75f477d83768a84e0f6fc7a.shtml (in Chinese).

Fan, J.L., Fu, J., Zhang, X., et al., 2023. Co-firing plants with retrofitted carbon capture and storage for power-sector emissions mitigation. Nat. Clim. Change 13 (8), 807–815. https://doi.org/10.1038/s41558-023-01736-y.

Gan, L., Yang, T., Chen, X., et al., 2023. Low-carbon scheduling of integrated energy system in iron & steel industrial Park considering low-carbon techniques and process control. Power Syst. Technol. 47 (8), 3099–3110. https://doi.org/10.13335/j.1000-3673.pst.2023.0481 (in Chinese).

Gu, H., Li, Y., Yu, J., et al., 2020. Bi-level optimal low-carbon economic dispatch for an industrial park with consideration of multi-energy price incentives. Appl. Energy 262, 114276. https://doi.org/10.1016/j.apenergy.2019.114276.

Halabi, M.A., Al-Qattan, A., Al-Otaibi, A., 2015. Application of solar energy in the oil industry—Current status and future prospects. Renew. Sustain. Energy Rev. 43, 296–314. https://doi.org/10.1016/j.rser.2014.11.030.

Hu, H., Sun, X., Zeng, B., et al., 2022. Enhanced evolutionary multi-objective optimization-based dispatch of coal mine integrated energy system with flexible load. Appl. Energy 307, 118130. https://doi.org/10.1016/j.apenergy.2021.118130.

IEA, 2023. The Oil and Gas Industry in Net Zero Transitions - Analysis. https://www.iea.org/reports/the-oil-and-gas-industry-in-net-zero-transitions.

IPCC, 2023. In: Climate Change 2023: Synthesis Report. Contribution of Working Groups I, II and III to the Sixth Assessment Report of the Intergovernmental Panel on Climate Change. IPCC, Geneva, Switzerland, pp. 35–115. https://doi.org/10.59327/IPCC/AR6-9789291691647.

James, J.A., Thomas, V.M., Pandit, A., et al., 2016. Water, air emissions, and cost impacts of air-cooled microturbines for combined cooling, heating, and power systems: a case study in the Atlanta region. Engineering 2 (4), 470–480. https://doi.org/10.1016/J.ENG.2016.04.008.

Khan, A., Javaid, N., 2020. Jaya learning-based optimization for optimal sizing of stand-alone photovoltaic, wind turbine, and battery systems. Engineering 6 (7), 812–826. https://doi.org/10.1016/j.eng.2020.06.004.

Li, D., Cai, J., Arıcı, M., et al., 2024a. Operational characteristics of solar-gas combined heating water system with phase change heat storage units for oilfield hot water stations. Energy 302, 131812. https://doi.org/10.1016/j.energy.2024.131812.

Li, D., Wang, Z., Wu, Y., et al., 2024b. Combined solar and ground source heat pump heating system with a latent heat storage tank as a sustainable system to replace an oilfield hot water station. Energy 307, 132726. https://doi.org/10.1016/j.energy.2024.132726.

Li, R., Ren, H., Wu, Q., et al., 2024. Cooperative economic dispatch of EV-HV coupled electric-hydrogen integrated energy system considering V2G response and carbon trading. Renew. Energy 227, 120488. https://doi.org/10.1016/j.renene.2024.120488.

Li, X., Chen, L., Hao, Y., et al., 2023. Sharing hydrogen storage capacity planning for multi-microgrid investors with limited rationality: a differential evolution game approach. J. Clean. Prod. 417, 138100. https://doi.org/10.1016/j.jclepro.2023.138100.

Li, Z., Wu, W., Shahidehpour, M., et al., 2015. Combined heat and power dispatch considering pipeline energy storage of district heating network. IEEE Trans. Sustain. Energy 7 (1), 12–22. https://doi.org/10.1109/TSTE.2015.2467383.

Li, Z., Zhao, W., Li, W., et al., 2025. Energy transition scheme for the integration of oil and gas with new energy based on hybrid methods. Energy Convers. Manag. 343, 120212. https://doi.org/10.1016/j.enconman.2025.120212.

Lin, J., Cai, R., 2023. Optimal planning for industrial park-integrated energy system with hydrogen energy industry chain. Int. J. Hydrogen Energy 48 (50), 19046–19059. https://doi.org/10.1016/j.ijhydene.2023.01.371.

Lin, J., Hu, G., Sun, Z., et al., 2025. Capacity configuration of a multi-energy complementary integrated energy system in a mining area based on multi-objective optimization. J. China Coal Soc. 1–12. https://doi.org/10.13225/j.cnki.jccs.2025.1018 (in Chinese).

Liu, H., Fu, Z., Huang, Q., et al., 2023. Experimental investigation on continuous reaction crystallizer for CO_2 capture by phase-change method. Chem. Eng. J. 466, 143345. https://doi.org/10.1016/j.cej.2023.143345.

Liu, Z.F., Zhao, S.X., Luo, X.F., et al., 2025. Two-layer energy dispatching and collaborative optimization of regional integrated energy system considering stakeholders game and flexible load management. Appl. Energy 379, 124918. https://doi.org/10.1016/j.apenergy.2024.124918.

Lu, Q., Chen, T., Wang, H., et al., 2014. Combined heat and power dispatch model for power system with heat accumulator. Electr Power Automat Equ 34, 79–85. https://doi.org/10.3969/j.issn.1006-6047.2014.05.012 (in Chinese).

Lu, S., Fang, M., Li, Q., et al., 2021. The experience in the research and design of a 2 million tons/year flue gas CO_2 capture project for coal-fired power plants. Int. J. Greenh. Gas Control 110, 103423. https://doi.org/10.1016/j.ijggc.2021.103423.

Ma, J., Li, L., Wang, H., Du, Y., Ma, J., Zhang, X., et al., 2022. Carbon capture and storage: history and the road ahead. Engineering 14, 33–43. https://doi.org/10.1016/j.eng.2021.11.024.

Ma, T., Li, M.J., Fan, C.H., et al., 2024. A novel real-time dynamic performance evaluation and capacity configuration optimization method of generation-storage-load for integrated energy system. Appl. Energy 374, 123896. https://doi.org/10.1016/j.apenergy.2024.123896.

Machado, A.A.P., Fiorotti, R., Villaça, R.S., et al., 2024. Profit distribution through blockchain solution from battery energy storage system in a virtual power plant using intelligence techniques. J. Energy Storage 98, 113150. https://doi.org/10.1016/j.est.2024.113150.

Mancarella, P., 2014. MES (multi-energy systems): an overview of concepts and evaluation models. Energy 65, 1–17. https://doi.org/10.1016/j.energy.2013.10.041.

Peng, C., Zhao, X., Deng, W., et al., 2025. An optimal scheduling method for oilfield integrated energy system considering source-load uncertainty. J Northeast Petrol Univer 49 (1). https://doi.org/10.3969/j.issn.2095-4107.2025.01.008 (in Chinese).

Qian, J., Wu, J., Zhang, Z., et al., 2025. Towards near-zero carbon: low-carbon evolution and planning of time-regulated park integrated energy system. Energy, 138591. https://doi.org/10.1016/j.energy.2025.138591.

Qin, X., Sun, H., Shen, X., et al., 2019. A generalized quasi-dynamic model for electric-heat coupling integrated energy system with distributed energy resources. Appl. Energy 251, 113270. https://doi.org/10.1016/j.apenergy.2019.05.073.

Rochelle, G.T., 2009. Amine scrubbing for CO_2 capture. Science 325 (5948), 1652–1654. https://doi.org/10.1126/science.1176731.

Sarker, E., Seyedmahmoudian, M., Jamei, E., et al., 2020. Optimal management of home loads with renewable energy integration and demand response strategy. Energy 210, 118602. https://doi.org/10.1016/j.energy.2020.118602.

Shell Petroleum, 2023. 2022 Energy Transition Progress Report. https://www.shell.com/sustainability/reporting-centre/reporting-centre-archive.html#tab-2022.

Sima, Q., Yang, S., Bao, Y., 2024. Net load forecasting and dynamic power dispatch considering the synergistic control of carbon emissions and air pollution. Chinese J Manag Sci 1–16. https://doi.org/10.16381/j.cnki.issn1003-207x.2023.1826.

Total Energy, 2022. 2022 Strategy and Outlook Report. https://totalenergies.com/system/files/documents/2022-09/TotalEnergies_2022_Strategy_and_Outlook_presentation.pdf.

Wang, R., Cai, W., Cui, R.Y., Huang, L., Ma, W., Qi, B., et al., 2025. Reducing transition costs towards carbon neutrality of China's coal power plants. Nat. Commun. 16, 241. https://doi.org/10.1038/s41467-024-55332-5.

Wang, T., Li, G., Song, X., Wang, H., Wang, G., Liu, Z., 2024a. Development of smart oil and gas fields with multi-energy synergy of wind, solar, geothermal, and energy storage. Strateg Study CAE 26 (4), 259–270. https://doi.org/10.15302/J-SSCAE-2024.04.004 (in Chinese).

Wang, Y., Luo, S., Miao, R., Ni, C., Yi, J., 2024b. Optimal planning of oilfield integrated energy system based on interval theory. Electr Power Automat Equ 44 (3). https://doi.org/10.16081/j.epae.202305010 (in Chinese).

Wang, Y., Song, Y., Ni, C., Yi, J., Zou, P., 2022. Cooperative peak load regulation ability analysis of thermal power plant and demand response for oil field integrated energy system with photovoltaic. Electr Power Automat Equ 42 (7), 198–204. https://doi.org/10.16081/j.epae.202202014 (in Chinese).

Xu, F., Song, X., Song, G., et al., 2023. Numerical studies on heat extraction evaluation and multi-objective optimization of abandoned oil well patterns in intermittent operation mode. Energy 269, 126777. https://doi.org/10.1016/j.energy.2023.126777.

Yang, L., Wei, N., Lv, H., et al., 2022. Optimal deployment for carbon capture enables more than half of China's coal-fired power plant to achieve low-carbon transformation. iScience 25 (12). https://doi.org/10.1016/j.isci.2022.105664.

Zhang, A., Zheng, Y., Huang, H., et al., 2022. Co-integration theory-based cluster time-varying load optimization control model of regional integrated energy system. Energy 260, 125086. https://doi.org/10.1016/j.energy.2022.125086.

Zhang, Q., Liu, J.F., Gao, Z.H., et al., 2023a. Review on the challenges and strategies in oil and gas industry's transition towards carbon neutrality in China. Pet. Sci. 20 (6), 3931–3944. https://doi.org/10.1016/j.petsci.2023.06.004.

Zhang, Q., Liu, J., Wang, G., et al., 2024. A new optimization model for carbon capture utilization and storage (CCUS) layout based on high-resolution geological variability. Appl. Energy 363, 123065. https://doi.org/10.1016/j.apenergy.2024.123065.

Zhang, Q., Zhang, H., Yan, Y., et al., 2021. Sustainable and clean oilfield development: how access to wind power can make offshore platforms more sustainable with production stability. J. Clean. Prod. 294, 126225. https://doi.org/10.1016/j.jclepro.2021.126225.

Zhang, W., Wang, W., Wang, H., et al., 2023b. Optimal capacity configuration for wind power-photovoltaic and oxygen-enriched coal-fired power generation system considering carbon capture technology. Autom. Electr. Power Syst. 47 (13), 176–189. https://doi.org/10.7500/AEPS20230227007 (in Chinese).

Zhang, Z.H., Zhang, Z.Y., Zhang, X.J., et al., 2023c. Optimal operation regulation strategy of multi-energy complementary system considering source load storage dynamic characteristics in oilfield well sites. Elec. Power Syst. Res. 225, 109799. https://doi.org/10.1016/j.epsr.2023.109799.

Zhao, W., Shao, Z., Yang, S., Lu, X., 2025. A novel conditional diffusion model for joint source-load scenario generation considering both diversity and controllability. Appl. Energy 377, 124555. https://doi.org/10.1016/j.apenergy.2024.124555.